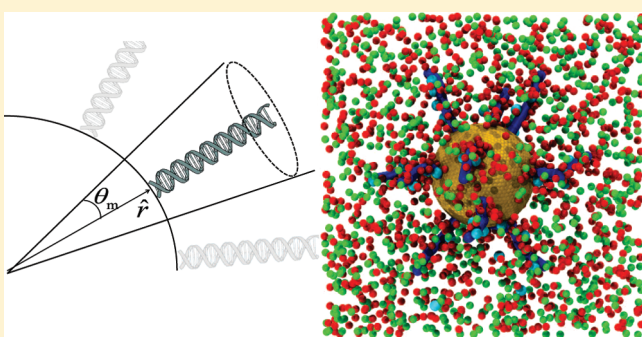


Local Ionic Environment around Polyvalent Nucleic Acid-Functionalized Nanoparticles

Jos W. Zwanikken, Peijun Guo, Chad A. Mirkin, and Monica Olvera de la Cruz*

Department of Materials Science and Engineering, Northwestern University, 2220 Campus Drive, 60208 Evanston, Illinois, United States

ABSTRACT: Polyvalent oligonucleotide-functionalized gold nanoparticles are remarkably stable in a cellular environment against degradation by nucleases, a property that was recently attributed to the local high concentration of mono- and divalent ions. To evaluate this hypothesis in more detail, we investigate the composition of the ion cloud around spherical nanoparticles that are functionalized by stiff, highly charged polyelectrolyte chains by means of classical density functional theory and molecular dynamics simulations. We present a cell model that includes ligands explicitly and both applies over the entire relevant parameter space and is in excellent quantitative agreement with simulations. We study the ion cloud for varying oligonucleotide grafting densities and bulk ionic concentrations, as well as different sizes of nanoparticles and chains, and distinguish a parameter regime where many-body interactions between the ligands have a dominant effect on the local environment. For small particles with high oligonucleotide surface densities, we find strongly enhanced local salt concentrations, a large radial component of the electric field between the ligands, and a pronounced localization of divalent ions near the surface of the nanoparticle, thus providing multiple supporting arguments for the hypothesis.



INTRODUCTION

Gold nanoparticles that are densely functionalized with oligonucleotide chains (DNA-AuNP) have been utilized for a wide variety of applications, which exploit the combined optical and electronic properties of the metal core with the highly selective recognition properties of the DNA ligands. DNA-AuNPs are synthetically programmable, can be used to make discrete crystal lattices and polymers with deliberately designed particle periodicities,^{1,2} are the basis for ultrasensitive chemical and biological detection methods,^{3,4} and have exhibited promise as potent intracellular gene regulation agents.^{5,6} With an increasing number of applications and possibilities in a high-dimensional parameter space, the formulation of predictive theoretical models may become useful for optimization, for providing experimental direction, and for the quantification of important structure–function relationships for the particles.

General control parameters in applications of DNA-AuNPs include the type and concentration of electrolytes that mediate the interactions between the highly charged oligonucleotide linkers. High salt concentrations typically increase the melting temperatures of duplex linkers⁸ and, therefore, the binding affinity of single strands with complementary nucleic acids. They also appear to be responsible, in part, for the nuclease resistance of the particles compared to molecular oligonucleotides.⁷ Moreover, the length and local density of the ligands as well as the size of the nanoparticle all appear to be influential factors.⁸ Motivated by these recent observations, we constructed a theoretical model

and also performed molecular dynamics (MD) simulations, which explicitly take into account the ligands, to obtain detailed estimates of the local salt concentrations and to correlate the results with the characteristic properties of DNA-AuNPs. The theoretical method is computationally efficient over the entire relevant parameter space, converging in seconds on a single CPU and is in excellent agreement with the results from MD simulations that are only feasible for a very limited set of parameters. We quantify the local concentration and composition of the screening cloud and calculate the entropy-induced local electric field. For small particles modified with dense layers of oligonucleotides, both methods predict elevated salt concentrations, divalent ion localization, and a strong electric-field component parallel to the chains. We argue that the locally elevated concentrations of salt, together with the strong localization of divalent ions and confinement near the nanoparticle surface, have a significant effect on protein functionality and provide an unfavorable environment for catalysis in the case of salt-sensitive enzymes (e.g., DNase I).

THEORY

The full molecular details of dsDNA provide great challenges for both theoretical modeling and computations, and the attempt for solutions led to coarse-grained models^{9,10} that reduce

Received: June 14, 2011

Revised: July 20, 2011

Published: July 24, 2011

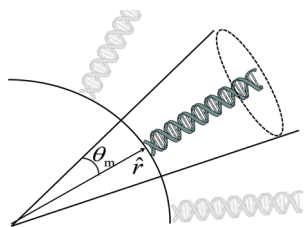


Figure 1. 2-dimensional projection of the sphere together with one Voronoi cell. The cells are approximated by azimuthally symmetric cones to simplify the electrostatic boundary conditions.

computational efforts. For our case of interest, we focus on rod-like, highly charged stiff chains, with properties that are inspired by those of dsDNA such as bending rigidity and charge density. We choose not to consider the complex molecular structure of dsDNA that, while being potentially responsible for distinctive quantitative effects, could also obscure the more general electrostatic effects in functionalized nanoparticles. Using symmetry arguments to reduce our problem to a single chain in a conical Wigner–Seitz cell, we study the local salt densities by means of a modified Poisson–Boltzmann (PB) model, which is derived within the framework of density functional theory (DFT), and compare with the results from MD simulations. PB cell models have been used extensively to study charged spheres,¹² and rods,^{13,14} in systems of cells with identical geometries, and yielded information about the effect of electrostatic screening for a broad range of thermodynamic conditions. The well-known Yukawa potential, typically decaying over the Debye length κ^{-1} , can be derived straightforwardly from the linearized PB equation acceptable for weakly charged spheres. It also describes accurately the long tail of the mean electrostatic potential around highly charged spheres after a renormalization of the particle charge.¹⁵ The full nonlinear solution deviates from the (renormalized) Yukawa potential at short ranges $<\kappa^{-1}$, in the so-called Stern layer, which depends on the charge of the particle, valency of the ions, and permittivity of the medium, as well as the cell size (inverse particle density). We found identical effects for a system of highly charged chains with one attached end to the surface of an uncharged sphere, albeit in a more complicated context and also depending on additional parameters such as the chain length, chain thickness, surface curvature, and grafting density, which are all relevant control parameters in experiments. Additional distinguishing effects were found, for example, concerning the *radial* decay of the screening cloud that appeared dependent on the *width* of the chains.

Apart from being motivated by recent applications of DNA–AuNPs, we found the typical material parameters highly inviting for a systematic theoretical analysis, because they allow for convenient simplifications in the model and in the numerical evaluation. In contrast to successful approaches for polyelectrolyte brushes,^{16,17} we can ignore the aspect of flexibility, which is irrelevant for the short dsDNA strands of interest, and can consider the spatial composition in more detail. Moreover, simulation methods with explicit ions are severely limited due to the charge density of dsDNA and the salt concentrations of interest and would be unsuitable for densely functionalized nanoparticles larger than ~ 10 nm. To make a comparison with MD simulations, we consider spherical nanoparticles with a radius $a = 3.35$ nm typically, comparable to the length $l = 5$ nm of rod-like chains with a high persistence length $l_p \gg l$,

which are connected with one end to the surface of the sphere. The effective radii of the ions $a_s = 0.3$ nm are taken to be equal for all components (with valencies $+1$, -1 , and $+2$). We consider Na^+ and Cl^- ions at typical buffer concentrations of 0.1 M and Ca^{2+} ions at 0.001 M, inspired by experimental conditions, though also analyze the system for a broad range of NaCl concentrations. The surrounding water is modeled as a structureless, homogeneous dielectric background medium with permittivity $\epsilon = 78.9$ (relative to vacuum), which dielectrically screens the Coulomb interaction between two monovalent ions to values of $\sim \pm 1 k_B T$ at contact. The number of chains per nanoparticle N_c are varied, such that the surface coverage $\sigma_c = N_c/4\pi a^2$ ranges between $0.01 \approx \sigma_c \approx 0.3 \text{ nm}^{-2}$ (between 1 and 50 pmol/cm^2). The density of negative charges on the chains is taken to be fixed at 6 nm^{-1} , which corresponds to the number of charged groups on the backbone of dsDNA, and for similar reasons we fix the persistence length to $l_p \sim 20$ nm, which is the value obtained for short dsDNA fragments in simulations.¹⁰ Moreover, though the reported persistence of dsDNA at 0.1 M NaCl is around 50 nm, in the presence of divalent ions it can be reduced to 20 – 30 nm¹¹ due to the short-range attractions induced by condensed divalent ions, which our coarse-grained model does not include. In either case one can expect the chains to behave as highly rigid for the short chain lengths of interest. The non-Coulombic interactions between the ions and the chains are differently treated in the theoretical approach and the simulations. The chains are considered as a permeable cloud of charges in the theoretical model but are considered as impenetrable by a Lennard-Jones repulsion in the simulations, whereas a strand of dsDNA may have characteristics that lie between these two extremes. In the theoretical model we make use of symmetry arguments to reduce the number of degrees of freedom. The nanoparticle is placed at the origin of a spherical coordinate system, and the chains are homogeneously distributed across the surface. We subdivide space into cells of more or less equal volume by means of a Voronoi construction, such that every cell contains exactly one chain, and assume that the electric field vanishes at the boundary. We then align the coordinate system such that \hat{r} points to a position where a chain is attached for $\theta = 0$, approximate the cell geometry by a cone such that two degrees of freedom (r, θ) are left, and assume that all cells are identical (Figure 1). The maximal angle θ_m is set by the total number of chains, $\cos \theta_m = 1 - 2/N_c$, to conserve the surface area per chain $1/\sigma_c$. The total system including the ions is considered to be in contact with a heat and salt bath, i.e., as a grand canonical ensemble. From a grand canonical density functional we calculate the expectation value of the ion densities ρ_α , and electrostatic potential ϕ , as described in the Methods.

METHODS

We construct a density functional $\Omega[\{\rho\}]$ that reduces to the grand potential of the system for the equilibrium densities $\{\rho_{\text{eq}}\}$ that minimize the functional, according to the principles of DFT. In a mean field approximation for the Coulombic interactions, we write the functional as

$$\beta\Omega[\{\rho\}] = \beta\Omega_{\text{id}}[\{\rho\}] + \frac{1}{2} \int d\mathbf{r} \phi(\mathbf{r}) Q(\mathbf{r}) + \beta F_{\text{exc}}^{\text{CS}}[\{\rho\}] \quad (1)$$

with $\beta = 1/k_B T$. The first term, the ideal grand potential functional, obeys

$$\beta\Omega_{\text{id}}[\{\rho\}] = \sum_{\alpha=+, -, 2+} \int d\mathbf{r} \rho_{\alpha}(\mathbf{r}) \left(\ln \frac{\rho_{\alpha}(\mathbf{r})}{\rho_{\alpha,s}} - 1 \right) \quad (2)$$

with $\rho_{\alpha,s}$ the reservoir density of species α . The second term in eq 1 is the electrostatic contribution, which includes the self-consistent electrostatic potential $\beta e\phi(\mathbf{r})$, with e the elementary charge, and total charge density eQ , with $Q(\mathbf{r}) = \rho_+(\mathbf{r}) - \rho_-(\mathbf{r}) + 2\rho_{2+}(\mathbf{r}) - \rho_c(\mathbf{r})$. The charge density of the chains $e\rho_c$ is assumed to be a fixed distribution, with a cylindrical geometry of a typical width equal to $a_c + a_s$, where a_c is the radius of the chain. The third contribution in (1) is the Carnahan–Starling excess free energy functional, corresponding to a local density approximation of the contribution due to hard core interactions,

$$\beta F_{\text{exc}}^{\text{CS}}[\{\rho\}] = \int d\mathbf{r} \rho(\mathbf{r}) \frac{4\eta(\mathbf{r}) - 3\eta(\mathbf{r})^2}{(1 - \eta(\mathbf{r}))^2} \quad (3)$$

with total density $\rho(\mathbf{r}) = \rho_+(\mathbf{r}) + \rho_-(\mathbf{r}) + \rho_{2+}(\mathbf{r})$ and total packing fraction $\eta(\mathbf{r}) = 4\pi a_s^3 \rho(\mathbf{r})/3$. The equilibrium profiles are obtained by a functional minimization of (1) with respect to the salt densities

$$\rho_{\pm}(\mathbf{r}) = \rho_s \exp(\mp \phi(\mathbf{r}) - \mu_{\text{exc}}^{\text{CS}}[\{\rho\}]) \quad (4)$$

in terms of ϕ that is obtained self-consistently by the Poisson equation

$$\nabla^2 \phi(\mathbf{r}) = -4\pi l_B Q(\mathbf{r}) \quad (5)$$

with boundary conditions

$$\begin{aligned} \lim_{r \rightarrow \infty} \frac{\partial \phi(r, \theta)}{\partial r} &= \lim_{r \downarrow a} \frac{\partial \phi(r, \theta)}{\partial r} = 0 \\ \lim_{\theta \uparrow \theta_m} \frac{\partial \phi(r, \theta)}{\partial \theta} &= \lim_{\theta \downarrow 0} \frac{\partial \phi(r, \theta)}{\partial \theta} = 0 \end{aligned} \quad (6)$$

Equations 4 and 5 are solved on an (r, θ) grid, by an iterative method that typically converges within several seconds on a single CPU.

The simulation method considers a spherical particle fixed at the origin of a box, covered with stiff chains that are immobilized at distinct positions to obtain a homogeneous distribution, surrounded by positive, negative, and divalent ions. The nanoparticle is composed of 92 beads at a distance a from the origin that tile the surface regularly¹⁹ (with indistinguishable results compared to a perfectly spherical particle of radius a). The hard-core interactions between the ions, between the ions and the nanoparticle surface, and between the ions and the chains are described by a 12,6 Lennard-Jones potential with a cutoff at its minimum that is shifted to zero. The electrostatic interactions are calculated by a particle–particle–mesh (PPPM) Ewald-sum method, implemented in the LAMMPS algorithm.¹⁸ The chains have a variable radius a_c and consist of typically 30 beads with an electrostatic charge of $-e$, separated by a distance $l_0 \approx 0.17$ nm, such that the line charge is $-6e/\text{nm}$, equal to that of dsDNA. We note that experimentally a larger charge density has been measured for grafted oligonucleotides (close to $-8e/\text{nm}$). In the future we will analyze larger charge densities and persistence lengths, but we do not expect qualitatively different behavior. The elastic properties and stiffness

Table 1. Parameter Sets Used in Theory (DFT) and Simulations (MD)

parameter name	symbol	set 1 (DFT)	set 2 (MD)	unit (alternative)
np radius	a	2–200	3.35	nm
dsDNA length	l	4.95–9.9 (15–30)	4.95 (15)	nm (base pairs)
NaCl buffer	c_s	0.001–1	0.1, 0.5	M
Ca ²⁺ buffer		0.001		M
grafting density	σ	0.02–0.3	(4, 6, 8, 12, 20)	nm ⁻² (no./NP)
chain radius	a_c	0.25–1.2	0.125–0.94	nm

of the chain are governed by the potentials

$$V_{\text{bond}}(l) = k_l(l/l_0 - 1)^2 \quad V_{\text{bend}} = k_{\varphi}(\varphi - \pi)^2 \quad (7)$$

respectively, with $k_l = 75k_B T$ and $k_{\varphi} = 63k_B T$, such that the persistence length of the chain equals that of dsDNA in an aqueous 0.1 M NaCl solution, $l_p \approx 20$ nm. The angle between two bonds intersecting at a bead is denoted by φ . The particles are embedded in a box with periodic boundary conditions and a sufficient width to avoid image effects, of typically 20 nm at 0.5 M NaCl and 23 nm at 0.1 M NaCl. The mean concentration of Cl ions is fixed instead of the reservoir concentration in the grand canonical ensemble of the theoretical model. The concentrations at the boundary were always found to be close to the mean concentration. Typically, $\mathcal{O}(10^3)$ monovalent ions were included, and four divalent ions per chain. A steady state was obtained after approximately $\mathcal{O}(10^6)$ time steps, corresponding to several hours on a high performance computing system.

RESULTS

A broad parameter range was investigated, and special attention was paid to the parameter sets presented in Table 1. The first set includes typical parameter values of recent experiments⁷ to allow for direct comparisons between theory and observations. The second set is judiciously chosen to optimize the computational efficiency of the molecular dynamics simulations.

We calculate the distributions of the ions and find that the fixed charge distribution of the chains, Figure 2a, is screened by a counterion cloud with a width of the order of the Debye screening length $1/\kappa = 1/(8\pi l_B c_s)^{1/2}$, Figure 2b. For the chosen grafting density of 0.14 nm^{-2} the ion clouds overlap between the chains, especially close to the surface of the sphere, giving rise to a significant radial gradient of the salt concentration and an increased concentration in the shared region. At lower grafting densities $\lesssim 0.07 \text{ nm}^{-2}$ the ion clouds are well separated, such that the ligands are screened as if detached, without a radial gradient in the local densities, except for small effects near the end of the chains and near the position where they are immobilized. To quantify the profile of the screening cloud, and the effect of grafting density on the local salt concentration, we evaluate the radially and angularly averaged distribution functions, $g_{\alpha}(r)$ and $g_{\alpha}(\theta)$, respectively:

$$\begin{aligned} g_{\alpha}(r) &\equiv \frac{1}{A_r} \int d\theta \sin \theta \rho_{\alpha}(r, \theta) \\ g_{\alpha}(\theta) &\equiv \frac{1}{A_{\theta}} \int dr r^2 \rho_{\alpha}(r, \theta) \end{aligned} \quad (8)$$

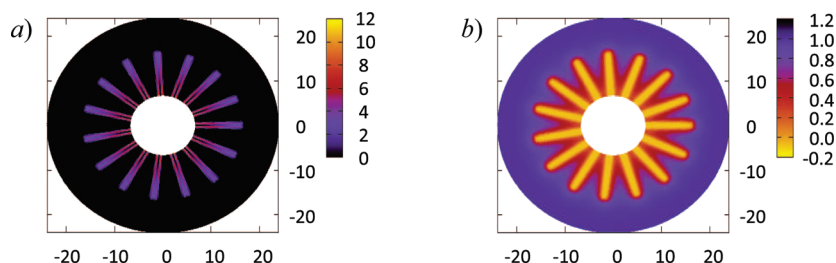


Figure 2. Charge density of chains (a) and the pNa (b) around a nanoparticle of radius $a = 6.5$ nm with a surface coating of $\sigma = 0.14 \text{ nm}^{-2}$ (24 pmol/cm²), with dsDNA chains of 30 base pairs, in the plane through the ($\theta = 0$) axis. The conical cell is mirrored until a full circle is obtained for a visualization of the full profile.

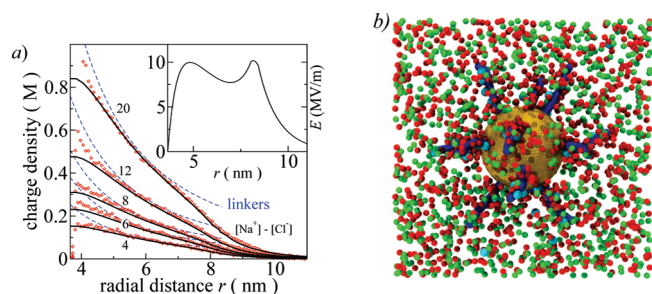


Figure 3. (a) Averaged radial distribution of the counterion cloud $[\text{Na}^+] - [\text{Cl}^-]$ from DFT (full curves) and simulations (symbols) and the charge density due to the linkers (dashed curves), for five different grafting densities (in units of linkers per nanoparticle, Table 1). The mean radial electric field, calculated by DFT, is shown in the inset. A simulation snapshot is shown in (b) with Na^+ in red, Cl^- in green, and Ca^{2+} in cyan, with very thin chains, in blue, on a small nanoparticle for transparency reasons. Na^+ and Ca^{2+} are dominantly present close to the chains. On average there are no Ca^{2+} -ions outside the corona of linkers.

with appropriate normalizing constants A_r and A_θ , and α denoting the ion species. A result from MD is shown in Figure 3a for the five grafting densities of the MD parameter set, at a salt concentration of 0.1 M, in the absence of Ca^{2+} . The dashed lines represent the charge distribution of the ligand; the full lines, the total charge density in the solvent $g_+(r) - g_-(r)$. The ion distributions smoothly decay near the end of the chains and near the surface and show a peak near the surface for the higher grafting densities, which we attribute to entropic and packing effects respectively. A snapshot from the corresponding simulation is shown in Figure 3b. The five curves can be collapsed onto a master curve, except for packing effects near the surface, given by

$$\bar{Q}_\alpha(r) = \frac{4\pi r^2}{N_c} g_\alpha(r) \quad (9)$$

where $\bar{Q}_\alpha(r) dr$ is the total number of ions of type α in a shell of width dr at position r . Four master curves are shown in Figure 4a corresponding to four different chain radii (parameter set 2), from simulations (symbols) and theory (solid lines). The dashed line marks the fixed, constant charge density of the chain. Clearly, the typical width of the screening cloud in the radial direction shows a dependency on the chain width; the thinner chains having a narrower screening layer. Results are similar in the presence of Ca^{2+} ions, except for the composition of the ion cloud, shown in Figure 4b. For a fixed bulk concentration of Ca^{2+} of 1 mM, the local concentration increases drastically with the grafting density above

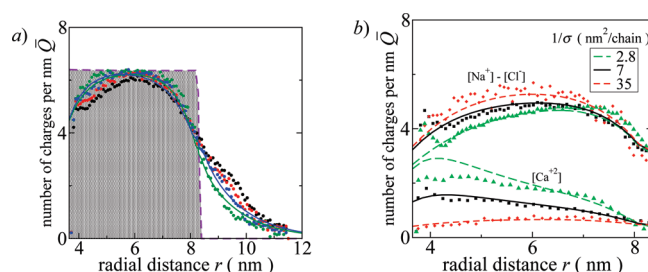


Figure 4. Mean number of charges per nanometer (a) on the chain (violet dashed line) and the number of compensating charges from DFT (continuous curves) and MD (dotted curves), for four different chain widths ranging from thin (green) to wide (black), as in Table 1. The mean number of compensating charges per nanometer for distances r within the layer of ligands is shown in (b), for low (red dashed curves) and high grafting densities (black continuous curves), for Ca^{2+} ions and counterions. The symbols are the results of MD simulations, and the curves are the results of the theory. Close quantitative agreement between the models is found up to unrealistically high grafting densities (green dashed line). For increasing grafting densities Ca^{2+} ions replace Na^+ ions especially close to the nanoparticle surface.

$\sigma \approx 0.05 \text{ nm}^{-2}$. Both methods are in quantitative agreement over the entire experimentally achievable range, except for excluded volume effects close to the surface. The increase of the average concentration around the nanoparticle (in the region $r < a + l$) is shown in Figure 5 as a function of grafting density σ (a), and bulk concentration of Na^+ (b), from MD simulations (symbols) and DFT (lines). The mean concentration of Ca^{2+} ions appears highly dependent on the grafting density σ , exceeding the bulk value by over 2 orders of magnitude for the highest σ . The local mean concentration of Na^+ shows less dramatic behavior than that of Ca^{2+} , yet it can exceed the bulk value up to a factor of 5. By decreasing the bulk concentration of Na^+ from $c_s = 0.5$ M to 1 mM while keeping that of Ca^{2+} fixed at 1 mM, the composition of the screening cloud is found to change drastically. Na^+ ions are replaced by Ca^{2+} ions until the latter dominate the screening layer below $c_s \approx 0.02$ M. At $c_s = 0.01$ M the local concentration of Ca^{2+} is twice as large as that of Na^+ , whereas it is 10 times lower in bulk. If the number of Ca^{2+} ions is kept fixed (dashed lines) instead of the bulk concentration, the local concentration is hardly dependent on c_s . The effect of the radius of curvature of the nanoparticle surface is demonstrated in Figure 6c. For a fixed σ , the mean concentration increases asymptotically to the value corresponding to a flat surface and decays for smaller radii, where the ends of the linkers separate due to the curvature. If we correct for the fact that smaller particles can sustain higher grafting densities, as observed by Hill et al.,²⁰ we

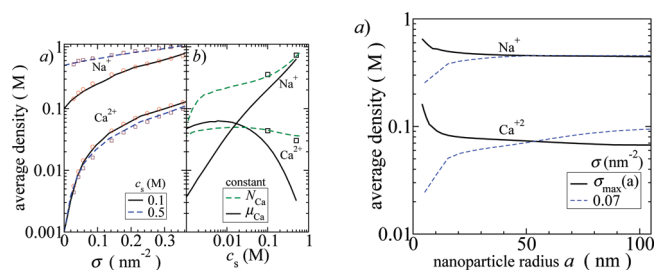


Figure 5. Local mean densities of Na⁺ and Ca²⁺ as a function of grafting density σ (a), reservoir concentration c_s (b), and nanoparticle radius a (c). The curves are results from the theoretical model, the symbols from MD simulations. In (a) the number of Ca²⁺ ions is fixed to four per chain, for a comparison between theory and the simulations. In (a), the chain radius $a_c = 0.5$ nm. In (b), $\sigma = 0.14$ nm⁻², and the theoretical results show results for both a constant number and constant buffer of 1 mM of Ca²⁺ ions. The results in (c) correspond to a constant grafting density σ (dashed), and to the maximal achievable $\sigma_{\max}(a)$ (continuous) as obtained from Hill et al.,²⁰ at fixed $c_s = 0.1$ M.

find the opposite trend; i.e., the local density is larger around smaller nanoparticles.

DISCUSSION AND CONCLUSION

The results from DFT calculations and MD simulations are in excellent agreement regarding the order parameters such as the mean radial density, the mean radial electric field, and the total average density, despite the differences in the modeling of the ligands. Most notable deviations are found in the ion density profiles close to the nanoparticle surface at high grafting densities when excluded volume effects can be distinguished, which are not contained in theory due to a local density approximation. These deviations are found to be small, though, for physiological salt conditions and experimentally achievable grafting densities.¹⁴ The electrostatic interactions between two oppositely charged ions are weak enough, $\approx -2k_B T$, to guarantee negligible correlations in bulk and near the chains, and we have not identified any persistent structure in the MD results. The agreement would probably be less satisfactory for tri- or polyvalent ions, or at extreme concentrations. Similar correlational effects can be expected near the polarizable surface of the AuNP, which may enhance the local concentration of ions close to contact, but probably negligible for the monovalent ions, and the activities of the Ca ions considered here. We thus present an efficient and accurate theoretical coarse-grained model for the study of the local ion concentrations around functionalized nanoparticles that includes the ligands explicitly and that is applicable over the entire relevant parameter space, typically converging in seconds on a single CPU, in contrast to the MD simulations, which were only feasible for minimal systems and required at least hours on a high performance computing system. The local environment induced by DNA-AuNPs can be characterized by strongly enhanced salt concentrations, by factors of 5 for monovalent and 2 orders of magnitude for divalent ions compared to the buffer, and electrostatic fields that have a large component parallel to the oligonucleotides of $\mathcal{O}(10)$ MV/m. The first can also be expected in dense concentrations of molecular DNA, although this may only be achievable in vivo by immobilization of the oligonucleotides on a nanoparticle surface. The second is a unique feature of DNA-AuNPs that is especially pronounced for

small particles $\lesssim 20$ nm. Consequences for local protein functionality, such as the inhibited activity of DNase I,⁷ seem unavoidable as it has been widely recognized to be dependent on the ionic environment and presence of external electric fields. The presence and localization of Ca²⁺ ions within the structure of DNase I have been shown to play a vital role for activity.^{21,22} The external fields generated by the ensemble of ligands are comparable to the local electric fields within the enzyme²³ and are expected to influence the structure as well. The large stiffness and high charge density of dsDNA contribute to a local environment where polymeric molecules may collapse due to high salt concentrations and strong electrostatic fields,¹⁶ to relax the local free energy density, where the oligonucleotides themselves remain robust. Another argument for the stability against degradation may be related to the dependence of the activity of DNase I on the specific binding site, as well as on the size of the helix grooves.²¹ The increased affinity of DNase I with DNA-AuNPs,⁷ which can be attributed to aspecific screening and salt-bridging effects,²⁴ may lead to enhanced, but inefficient, binding. These considerations are beyond the present model and are specific for this enzyme only. On the basis of the results of an effective and accurate theoretical method, we conclude that enzyme activity in general may be heavily influenced by the local environment around DNA-AuNPs, owing to the high charge density and robustness of dsDNA.

AUTHOR INFORMATION

Corresponding Author

*E-mail: m-olvera@northwestern.edu.

ACKNOWLEDGMENT

We thank Robert Macfarlane for valuable discussions and many useful suggestions. J.W.Z. was funded by the DDRE and AFOSR Award No. FA9550-10-1-0167, and P.G. by the Nonequilibrium Energy Research Center (NERC), which is an Energy Frontier Research Center funded by the U.S. Department of Energy, Office of Science, Office of Basic Energy Sciences under Award Number DE-SC0000989. M.O. and C.A.M. acknowledge the support of AFOSR MURI funded by DDRE.

REFERENCES

- (1) (a) Mirkin, C. A.; Letsinger, R. L.; Mucic, R. C.; Storhoff, J. J. *Nature* **1996**, 382, 607. (b) Elghanian, R.; Storhoff, J. J.; Mucic, R. C.; Letsinger, R. L.; Mirkin, C. A. *Science* **1997**, 277, 1078.
- (2) Macfarlane, R. J.; Jones, M. R.; Senesi, A. J.; Young, K. L.; Lee, B.; Wu, J.; Mirkin, C. A. *Angew. Chem., Int. Ed.* **2010**, 49, 4589.
- (3) Nam, J.-M.; Thaxton, C. S.; Mirkin, C. A. *Science* **2003**, 301, 1884.
- (4) Zheng, D.; Seferos, D. S.; Giljohann, D. A.; Patel, P. C.; Mirkin, C. A. *Nano Lett.* **2009**, 9, 3258.
- (5) Giljohann, D. A.; Seferos, D. S.; Daniel, W. L.; Massich, M. D.; Patel, P. C.; Mirkin, C. A. *Angew. Chem., Int. Ed.* **2010**, 49, 3280.
- (6) Prigodich, A. E.; Seferos, D. S.; Massich, M. D.; Giljohann, D. A.; Lane, B. C.; Mirkin, C. A. *ACS Nano* **2009**, 3, 2147.
- (7) Seferos, D. S.; Prigodich, A. E.; Giljohann, D. A.; Patel, P. C.; Mirkin, C. A. *Nano Lett.* **2009**, 9, 308.
- (8) Jin, R.; Wu, G.; Li, Z.; Mirkin, C. A.; Schatz, G. C. *J. Am. Chem. Soc.* **2003**, 125, 1643.
- (9) Sandberg, D. J.; Carrillo, J.-M. Y.; Dobrynin, A. V. *Langmuir* **2007**, 23, 12716.
- (10) Knotts, T. A.; Rathore, N.; Schwartz, D. C.; de Pablo, J. J. *J. Chem. Phys.* **2007**, 126, 084901.

- (11) Baumann, C.; Smith, S. B.; Bloomfield, V. A.; Bustamante, C. *Proc. Natl. Acad. Sci. U. S. A.* **1997**, *94*, 6185–6190.
- (12) von Grünberg, H.-H.; van Roij, R.; Klein, G. *Europhys. Lett.* **2001**, *55*, 580.
- (13) (a) Deserno, M.; von Grünberg, H.-H. *Phys. Rev. E* **2002**, *66*, 011401. (b) Deserno, M.; Holm, C.; May, S. *Macromolecules* **2000**, *33*, 199.
- (14) (a) Patra, C. N.; Yethiraj, A. *J. Phys. Chem. B* **1999**, *103*, 6080. (b) Patra, C. N.; Yethiraj, A. *Biophys. J.* **2000**, *78*, 699.
- (15) Alexander, S.; Chaikin, P. M.; Grant, P.; Morales, G. J.; Pincus, P.; Hone, D. *J. Chem. Phys.* **1984**, *80*, 5776.
- (16) Tagliazucchi, M.; Olvera de la Cruz, M.; Szleifer, I. *Proc. Natl. Acad. Sci. U. S. A.* **2010**, *107*, 5300.
- (17) Uline, M. J.; Rabin, Y.; Szleifer, I. *Langmuir* **2011**, *27*, 4679.
- (18) Plimpton, S. *J. Comput. Phys.* **1995**, *117*, 1 <http://lammps.sandia.gov>.
- (19) (a) Vernizzi, G.; Olvera de la Cruz, M. *Proc. Natl. Acad. Sci. U.S.A.* **2007**, *104*, 18382–86. (b) Vernizzi, G.; Sknepnek, R.; Olvera de la Cruz, M. *Proc. Natl. Acad. Sci. U. S. A.* **2011**, *108*, 4292.
- (20) Hill, H. D.; Millstone, J. E.; Banholzer, M. J.; Mirkin, C. A. *ACS Nano* **2009**, *3*, 418.
- (21) Suck, D.; Oefner, C. *Nature* **1986**, *321*, 620.
- (22) Kabsch, W.; Mannherz, H. G.; Suck, D.; Pai, E. F.; Holmes, K. C. *Nature* **1990**, *347*, 37.
- (23) Suydam, I. T.; Snow, C. D.; Pande, V. S.; Boxer, S. G. *Science* **2006**, *313*, 200.
- (24) Zwanikken, J. W.; Olvera de la Cruz, M. *Phys. Rev. E* **2010**, *82*, 050401(R).